PNAS RESEARCH ARTICLE | BIOPHYSICS AND COMPUTATIONAL BIOLOGY

Cooling fast and slow: Characterizing the effects of vitrification in cryo-EM and the subsequent recovery of equilibrium populations

Robert Clark[a,1], Louis G. Smith[b,1,2], Matthew P. Leighton[c,d], Ryan J. Szukalo[e], Syma Khalid[a], Pablo G. Debenedetti[f,3], Pilar Cossio[d,g], Miro A. Astore[d,g,3,4], and Sonya M. Hanson[d,g,3]

Affiliations are included on p. 11.

Contributed by Pablo G. Debenedetti; received June 4, 2026; accepted September 29, 2026; reviewed by Lars V. Bock, Helmut Grubmüller, and Vincent A. Voelz

Single-particle cryogenic electron microscopy (cryo-EM), a powerful class of techniques in structural biology with the potential to resolve molecular ensembles, requires that samples be vitrified to protect them from the high vacuum of the electron microscope. However, the effects of vitrification on biomolecular ensembles are unknown. To study them, we carried out extensive molecular dynamics simulations (over 50 ms) of the Trp-cage miniprotein at equilibrium and undergoing rapid cooling. We simulated seven cooling rates spanning three orders of magnitude, with the slowest coolings matching experimental rates. By inspecting molecular mobility and density-temperature trajectories for water with and without protein, we found that water vitrification is unaltered by the protein. To track protein conformation changes, and to relate them to kinetics, we made a Markov State Model (MSM) of Trp-cage from 5.4 ms of equilibrium sampling at 277 K. We observed that MSM states with a characteristic time longer than the duration of the nonequilibrium cooling tend to be more robust to artifacts induced by such cooling. Critically, although we observe that some states vanish in the equilibrium ensemble at 230 K, none do in our nonequilibrium cooled ensembles. To account for these perturbations, we developed a thermodynamic inference framework for recovering equilibrium populations from vitrified ensembles. These results indicate that cryo-EM has the capacity to be an accurate technique for the study of biomolecular ensembles.

molecular biophysics | nonequilibrium thermodynamics | cryo-EM | molecular dynamics

Significance

Cryogenic electron microscopy images biomolecules trapped in vitreous ice. The extent to which the required rapid cooling causes their ensemble to be perturbed from equilibrium is unknown. We use extensive molecular simulations to quantify the equilibrium dynamics of the Trp-cage miniprotein and the effects of cooling on its conformational ensemble. By simulating cooling at seven rates, including the slowest that still results in vitrification, we connect the kinetics of a protein's conformational state to its change in population from cooling. We show that cooling-induced population shifts are small but observable. We introduce a thermodynamic inference method to recover equilibrium populations from the cooled ensembles. This work provides a foundation for quantifying the perturbative effects of vitrification in cryogenic electron microscopy.

Elucidating the conformational changes biomolecules undergo is fundamental to understanding their function. Proteins, nucleic acids, and their complexes exist as dynamic ensembles, sampling multiple conformations that enable binding, catalysis, and regulation (1). Cryogenic electron microscopy (cryo-EM) is a transformative tool for structural biology, enabling near-atomic resolution structure determination of biomolecules without the need for crystallization (2). Single-particle analysis routinely resolves multiple distinct conformational states from the same sample (3), and emerging computational methods now aim to characterize continuous conformational landscapes and state populations (4, 5). It is often assumed that the ensemble imaged in cryo-EM resembles the equilibrium ensemble of the sample right before vitrification, however the validity of this assumption remains an open question (6, 7), limiting the insights one can gain from biomolecular conformations observed in cryo-EM data.

The high vacuum required for electron microscopy prevents the use of liquid-phase samples, and so cryo-EM relies on plunge-vitrification into a cryogen, usually liquid ethane, for sample preparation. This technique cools the sample to below 90 K within microseconds (8, 9) (Fig. 1*A*). The rapid cooling prevents the formation of hexagonal ice, which strongly scatters electrons, disrupting imaging, and structurally damages the biomolecules (2). Instead, water molecules arrest into low-density amorphous ice (LDA) (10, 11), a metastable glass that suspends macromolecules in a rigid, electron-transparent matrix (12). In 1988 Jaques Dubochet, one of the inventors of the vitrification process, published an estimate for the minimum cooling rate required to successfully vitrify water. By extrapolating from measurements of the fastest achievable cooling rate for thin specimens of tissue, Dubochet estimated that a cooling rate of 10^6 K/s could be achieved for a 1 μm thick film of water (2). This set the order of magnitude estimate for the critical cooling rate of water until the invention of an apparatus that allowed careful control of the vitrification process via laser mediated heating. With this more advanced instrumentation, the minimum cooling rate for vitrification has now been

Copyright © 2026 the Author(s). Published by PNAS. This article is distributed under Creative Commons Attribution-NonCommercial-NoDerivatives License 4.0 (CC BY-NC-ND).

[1]R.C. and L.G.S. contributed equally to this work.

[2]Present address: Center for Computational Biology, Flatiron Institute, New York, NY 10010.

[3]To whom correspondence may be addressed. Email: pdebene@princeton.edu, miro.astore@gmail.com, or shanson@flatironinstitute.org.

[4]Present address: Laboratory of RNA Structural Biology and Biophysics, The Rockefeller University, New York, NY 10065.

This article contains supporting information online at https://www.pnas.org/lookup/suppl/doi:10.1073/pnas.2619560123/-/DCSupplemental.

Published November 3, 2026.

Downloaded from https://www.pnas.org by PRINCETON UNIV LIBRARY; ACQUISITION SERVICE PERIODICALS on November 4, 2026 from IP address 140.180.240.79.

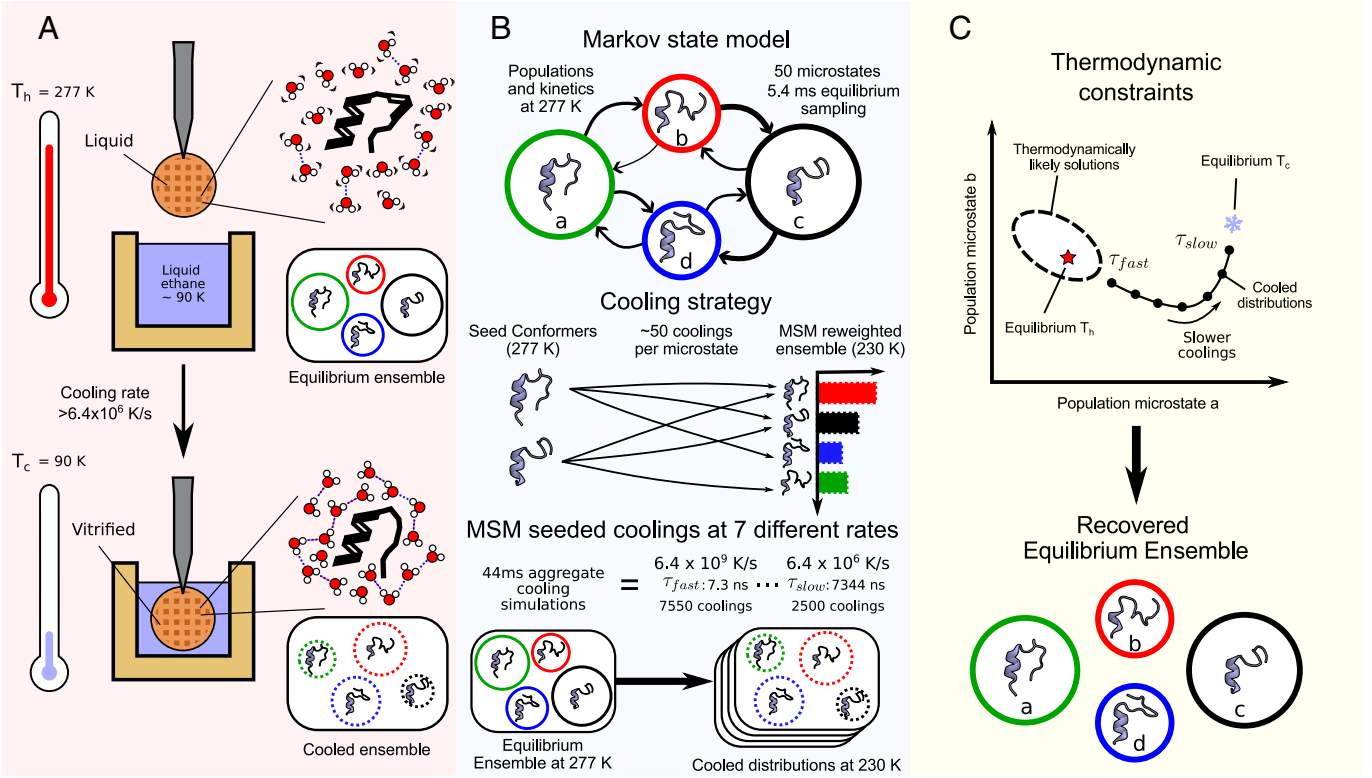


Fig. 1. Investigating and recovering from the effects of rapid vitrification on biomolecular conformations. (*A*) Cryo-EM relies on vitrification of solvated biomolecules to withstand high vacuum, immobilize, and preserve them. Samples are blotted onto a grid and plunged into liquid ethane, causing the solvent to transition into low-density amorphous ice (LDA). (*B*) The equilibrium ensemble at several temperatures was sampled through temperature replica exchange simulations, and the kinetics of the system at 277 K were estimated using a Markov State Model (MSM) built from equilibrium MD trajectories. To obtain vitrified ensembles for different cooling rates, we cooled conformers from each MSM state on average 50 times at seven different cooling rates, resulting in tens of thousands of cooling trajectories from 277 K to 230 K. By recording the MSM state identity of conformations before and after cooling, we estimate the abundance of postcooling states given their warm equilibrium populations.(*C*) Thermodynamic constraints provide bounds on the maximum perturbations that nonequilibrium cooling can have on the equilibrium ensemble. This shows how, as the cooling time increases, cooled distributions (black points) may move away from the hot equilibrium and toward the cold equilibrium. Thermodynamic constraints (dashed region) bound how far a hot equilibrium distribution consistent with these cooled distributions can lie from them. By combining a series of cooled ensembles, we found that these constraints are narrow enough to enable recovery of an equilibrium ensemble from the nonequilibrium cooled ensembles, in a process called thermodynamic inference.

precisely measured at 6.4×10^6 K/s, a number in agreement with Dubochet's estimate nearly 40 years earlier (9). At this cooling rate, cooling from 4 °C (~277 K) to past the glass transition (T_g) point at ~136 K occurs over approximately 22 μs, a timescale that overlaps with many biomolecular conformational transitions and binding events (14).

Conformational transitions with timescale comparable to the cooling duration could occur during vitrification, allowing populations to evolve away from the initial 277 K ensemble. Indeed, given sufficiently slow cooling, we would expect the ensemble to relax to the low temperature ensemble. Equilibrium conformational populations are known to shift at low temperature, with some proteins undergoing cold denaturation (15). At the other extreme, kinetic trapping could occur, where thermal fluctuations are not sufficient to permit equilibration of the system at all, which would retain the original equilibrium present prior to cooling. The extent of thermal relaxation possible during vitrification ought to determine the degree of resemblance between vitrified ensembles and those at 277 K. One can illustrate the complicated balance between kinetic trapping and thermal relaxation even using a simple 1D toy model (*SI Appendix*, Fig. S1). Simulating Langevin dynamics on a simple four-well potential undergoing rapid cooling shows how different barrier heights are overcome at different cooling rates. At fast rates, cooled ensembles still resemble the hot equilibrium, and are thus fully kinetically trapped, whereas for slow cooling the ensemble matches the cold equilibrium, since it has time to relax. We will refer to such relaxation accompanying slow cooling as annealing in what follows.

At intermediate cooling rates, the outcome is not a simple interpolation between these limits. Instead, the competition between kinetic trapping and annealing results in states that are enriched at one rate and depleted at another, while more stable states remain unchanged (*SI Appendix*, Fig. S1*B*). The complexity of outcomes seen even in this simple model motivates a full investigation of how a protein ensemble evolves under cooling at realistic cryo-EM cooling rates, and which properties make particular states more susceptible to change during vitrification. This is especially important given experimental evidence that the temperature prior to cooling influences the conformational distributions observed in cryo-EM (16, 17), consistent with both kinetic trapping or partial thermal relaxation during cooling, and in light of emerging time-resolved cryo-EM experiment where the achievable temporal resolution is approaching the vitrification timescale (18).

Computational methods are well-positioned to address how the balance of kinetic trapping and annealing changes the conformational distribution of a biomolecule during vitrification. For example, Bock and Grubmüller (19) performed molecular dynamics (MD) simulations of ribosome vitrification at cooling rates of 10^9 to 10^{11} K/s, demonstrating that energy barriers below approximately 10 kJ/mol can be traversed during cooling.

Downloaded from https://www.pnas.org by PRINCETON UNIV LIBRARY; ACQUISITION SERVICE PERIODICALS on November 4, 2026 from IP address 140.180.240.79.

However, these simulations used cooling rates that were unable to reach the range of slowest cooling rates that still result in vitrification. They also model the impact of cooling using a "largest-barrier" analysis suggesting that barriers higher than 10 kJ/mol were unlikely to be crossed in cooling. Given more recent experimental understanding of vitrification and recent results in stochastic thermodynamics that use constraints on entropy production in nonequilibrium processes for inference (20, 21), we can also now apply these approaches to the nonequilibrium cooling process that occurs in cryo-EM.

We found the need to move away from a characterization of the kinetics as emerging from a lone relevant barrier. Instead, to score the connectedness of a state in the kinetic network, we borrowed from existing stochastic thermodynamics literature on the dynamical activity in discrete-state Markov models (22) and define a characteristic time over which a given state exchanges probability with the rest of the network. We name it the event time. It gives the mean time required for 5% of the system's population to be exchanged to other states. This is a measure of gross probability traffic associated to a particular state. For details, see Eq. **1** and *Categorizing Change Under Cooling with Hot Equilibrium Kinetics*.

Here we combined extensive molecular simulation and approaches in stochastic thermodynamics to investigate perturbations to conformational ensembles introduced by vitrifaction and then recover the equilibrium distribution from the vitrified ensembles. Our system of choice is the Trp-cage miniprotein. Its small size (20 residues) permits exhaustive conformational sampling while exhibiting rich dynamics and thermodynamics, including microsecond timescale folding (23, 24) and cold denaturation (15, 25). We used the TIP4P/Ice water model, due to its overall accuracy, and in particular its parameterization so as to yield a realistic melting point (26, 27). We characterized the equilibrium landscape of Trp-cage at multiple temperatures and built a Markov state model (MSM) to describe the kinetics at 277 K. We ran tens of thousands of nonequilibrium cooling trajectories with conformations drawn from each microstate at experimentally realistic cooling rates (Fig. 1*B*) (9). By tracking the occupancy of MSM states before and after cooling, we analyze how a state's equilibrium kinetics influence its population changes under nonequilibrium cooling, and infer the general features of protein states beyond Trp-cage that influence behavior under cooling. We find that the population of a state may drift during cooling when the cooling time exceeds the event time, defined above.

Finally, we developed a framework for thermodynamic inference using constraints on entropy production during cooling to recover the original 277 K equilibrium distribution from the cooled distributions (Fig. 1*C*). Overall, these findings provide a robust framework to understand when states are disrupted by vitrification and how to correct for these cooling artifacts, both critical insights for the accurate interpretation of biomolecular ensembles recovered from cryo-EM samples.

Results

Hot and Cold Equilibrium Properties of the Trp-Cage System. To understand how rapid cooling affects biomolecular ensembles, we first characterized Trp-cage's properties at equilibrium. We performed temperature replica exchange (TREX) MD simulations spanning 230 K to 520 K using 90 replicas with 12 μs of sampling per replica for a total of 1.08 ms. We chose 230 K as our lowest temperature because in pilot nonequilibrium cooling simulations this temperature marked the onset of effective vitrification (*SI Appendix*, Fig. S2), where both conformational changes and water self-diffusion slow dramatically (*SI Appendix*, Fig. S3). The TREX revealed markedly different ensembles at 277 K versus 230 K (Fig. 2*A* and *SI Appendix*, Fig. S4). In what follows, we use "microstate" and "state" interchangeably to refer to the states of our Markov model.

At 277 K, Trp-cage predominantly populates the native folded conformations (states 10 and 23), consistent with experimental characterization (24). At 230 K, Trp-cage favors multiple cold-denatured conformations where the α-helix or the 3_{10}-helix begins to lose its structure (states 27, 39, 47, and 49). Trp-cage can sample diffusively (albeit very slowly) at 230 K (*SI Appendix*, section 1 and Fig. S3*A*), but at the cooling rates explored here the system falls out of equilibrium and 230 K can be considered as an effective glass transition temperature. Additionally, there are ten microstates in the 277 K ensemble which we do not sample in the 230 K ensemble (*SI Appendix*, Fig. S4). These temperature-dependent equilibrium shifts serve as fiducials for evaluating vitrification effects. That is, if the cooling were slow enough to allow full thermal relaxation, we would find that the populations after cooling match those from the equilibrium distribution at 230 K. Therefore, deviations from this distribution reflect the particulars of nonequilibrium cooling.

To quantify kinetics at 277 K and track conformational changes during cooling, we performed 5.4 ms of unbiased Trp-cage simulations with conformations seeded from across the 277 K TREX ensemble. We clustered and featurized trajectories using all rotatable dihedral angles reduced with time-lagged Independent Component Analysis (TICA) (28, 29). From these we built a Bayesian MSM with 50 microstates using a 40 ns lag time, and constrained the stationary distribution to the 277 K populations from TREX (*Materials and Methods*) (30). As the simulations were performed in explicit solvent, the model implicitly reflects solvated conformational preferences. The resulting kinetic network reveals the connectivity and transition rates between states (Fig. 2*B* and *SI Appendix*, Fig. S5). The MSM showed clear kinetic separation between different cold-denatured conformations and multiple similar but distinct folded states (*SI Appendix*, Fig. S6). The range of timescales provided a suitable range to relate the rate of cooling up to and including experimentally relevant states. To compare with the nonequilibrium cooling dynamics, we begin by asking whether water's behavior is perturbed in the protein and water system cooled using our sampling approach.

Bulk Solvent Vitrification Is Unperturbed by Protein Presence. To study the bulk solvent under cooling, we characterized water vitrification through molecular mobility and density-temperature equations of state. We found that neither the presence of the protein nor the cooling rate had a significant effect on the (T, ρ) pathway, which is indistinguishable from that in pure bulk water. Simulation snapshots where water molecules are color-coded by their displacement over 0.5 ps illustrate the progressive slowing of water dynamics upon cooling (Fig. 3*A*). At 277 K, water molecules exhibit large, thermally-driven displacements typical of a normal liquid. By 230 K, mobility has decreased substantially and dynamic heterogeneity emerges, with pockets of mobile water molecules coexisting alongside near-arrested ones, behavior characteristic of deeply supercooled liquids approaching vitrification. At 100 K, nearly all water molecules are immobile, with displacements reduced to small vibrations characteristic of glassy dynamics. Velocity

Downloaded from https://www.pnas.org by PRINCETON UNIV LIBRARY; ACQUISITION SERVICE PERIODICALS on November 4, 2026 from IP address 140.180.240.79.

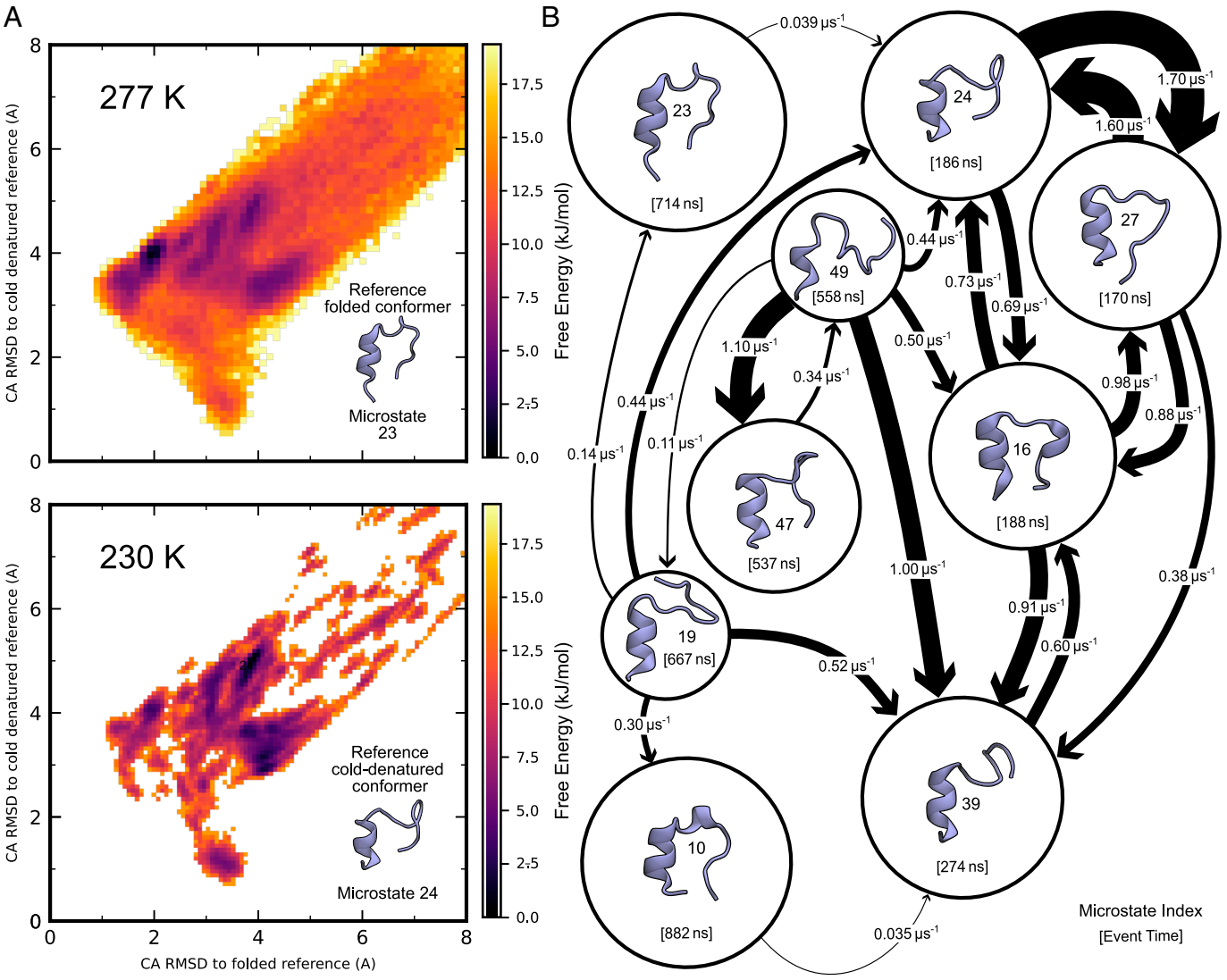


Fig. 2. Markov state model with 50 microstates describing the equilibrium conformational landscape of Trp-cage at 277 K and 230 K. (*A*) Free energy surfaces of Trp-cage at 277 K (*Top*) and 230 K (*Bottom*) from temperature replica exchange MD simulations. The coordinate axes show C_α RMSD to cold-denatured reference (y-axis) and C_α RMSD to folded reference (x-axis). Reference structures are shown *Inset*; see *SI Appendix*, Fig. S7 for cluster center locations on the landscape. (*B*) Markov state model connectivity graph showing transition rates between the nine states with probabilities greater than 1% at 277 K. Circle diameter is proportional to the log state population and the event time associated with each microstate is in square brackets. Arrow thickness is linearly proportional to the transition rate between states, with values labeled in μs^{-1}. Only transitions with rates $>0.3\ \mu s^{-1}$ are shown for visual clarity, except in cases where a rate below the cutoff was included to demonstrate that every state has in and out transitions.

autocorrelation functions further characterize this evolution in dynamics, showing increasingly oscillatory behavior upon cooling, and reveal that only the protein's first solvation shell exhibits dynamics distinct from bulk water, with the degree of this perturbation remaining largely independent of temperature (*SI Appendix*, Fig. S7).

To assess the thermodynamic pathway during cooling, we compared rate-dependent density-temperature trajectories for pure water and water in the presence of Trp-cage (Fig. 3*B*), extending cooling simulations to 80 K to fully characterize the glassy regime. For the Trp-cage simulations, the effective water density was computed by excluding the protein volume, taken as the volume occupied by spheres defined by the atomic van der Waals radii, from the simulation cell volume (*SI Appendix*, Fig. S8). At high temperatures, all cooling rates reproduce the equilibrium NPT density (open circles), confirming that the simulations are well-equilibrated at the onset of cooling. As temperature decreases, slower cooling rates track the equilibrium curve to lower temperatures before diverging, indicating that the system remains in equilibrium longer at slower rates. In all cases, the density reaches a minimum near 215 K before increasing as the system enters a glassy state, distinctive features of water's behavior and the formation of low-density amorphous ice (11). Critically, the density-temperature curves for Trp-cage-containing water are indistinguishable from pure water at all three cooling rates, with neither the density minimum nor the final glassy-state density affected by the miniprotein's presence.

Further, we calculated T_g for both pure water and the Trp-cage system at each cooling rate using a global hyperbolic fitting procedure (Fig. 3, *Inset*; see *SI Appendix*, section 1 and Fig. S3*A* for details) (31, 32). As expected, T_g decreased monotonically with decreasing cooling rate. Importantly, the T_g values with and without Trp-cage match at each cooling rate, showing that a single Trp-cage molecule in a periodic box of 3,240 water molecules does not measurably alter water vitrification.

Downloaded from https://www.pnas.org by PRINCETON UNIV LIBRARY; ACQUISITION SERVICE PERIODICALS on November 4, 2026 from IP address 140.180.240.79.

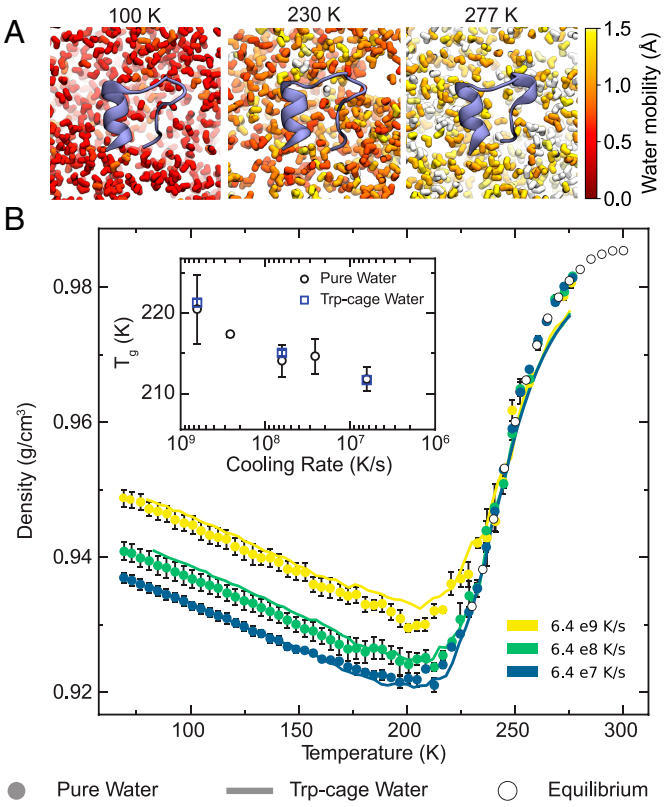


Fig. 3. Water vitrification dynamics and thermodynamics with and without protein. (*A*) Snapshots of water molecules colored by displacement over 0.5 ps at three temperatures (100 K, 230 K, and 277 K), showing progressive reduction in water mobility during cooling. Red indicates low mobility, white indicates high mobility. (*B*) Water density as a function of temperature during isobaric cooling at three different cooling rates. Filled circles represent pure water systems, while solid lines show water density in Trp-cage-containing systems (excluding protein volume). Open circles indicate equilibrium density values from NPT simulations. Colors distinguish cooling rates: 6.4×10^9 K/s (yellow), 6.4×10^8 K/s (green), and 6.4×10^7 K/s (blue). *Inset*: Glass transition temperature, T_g, as a function of cooling rate for pure water (circles) and Trp-cage systems (squares). Error bars represent SE of the mean across independent simulations.

These results establish that the presence of a small, compact biomolecule does not perturb either the thermodynamic pathway or the glassy dynamics of supercooled water during rapid cooling, and validate our choice of 230 K as the cooling endpoint for protein conformational analysis. By this temperature, water mobility has decreased substantially and the system, while still diffusive, approaches the glassy regime where conformational changes effectively cease. We further note that the glass-state densities reached in our slowest cooling simulations (Fig. 3*B*) approach the experimentally measured density of LDA (0.94 g/cm^3) (33). Having established that water's approach to vitrification proceeds normally in the presence of protein, we proceed to investigate the protein conformations as a function of cooling.

The Influence of Cooling on the Conformational Ensemble of a Protein. Having characterized the equilibrium landscape and kinetics of the Trp-cage system, we employed a shooting strategy to sample the effect of cooling on the conformational ensemble at seven cooling rates spanning three orders of magnitude, from 6.4×10^9 K/s (duration of 7.3 ns) up to the critical cooling rate of 6.4×10^6 K/s (duration of 7.3 μs) (9), accumulating 44 ms of sampling (*SI Appendix*, Table S1). For each cooling rate, we started collections of simulations from conformers obtained by geometric clustering of the TREX samples (*Materials and Methods*).

One might suppose that perturbations in protein state populations induced by cooling could yield an ensemble similar to an equilibrium ensemble at some temperature between the starting hot temperature and finishing cold temperature. To test this, we computed the Kullback–Leibler (KL) divergence between equilibrium populations at each temperature from the TREX simulations and the distributions resulting from cooling (cooled distributions) (Fig. 4*A*). For all cooling rates, the equilibrium distribution at 277 K remains the closest match to the cooled ensemble, with KL divergence increasing monotonically for lower temperatures.

Cooling induces modest but measurable population shifts in the most populous states (Fig. 4*B*). At the fastest cooling rate (6.4×10^9 K/s), populations remain indistinguishable from their 277 K equilibrium values for all nine states with abundance greater than 1%. As cooling slows, certain states exhibit systematic deviations. For instance, state 10, a folded state comprising 16.5% of the 277 K equilibrium, decreases to 12.7% at the critical cooling rate. However, in some cases states do not move toward their equilibrium population at 230 K (e.g state 49). We also observed nonmonotonic population change (for example, *SI Appendix*, Fig. S9*A* states 8, 38, 46). This is consistent with the behaviors of our toy model (*SI Appendix*, Fig. S1). Despite these changes, all states remain populated even at the slowest cooling rate. However, at equilibrium there are ten zero population states at 230 K (*SI Appendix*, Fig. S4). This result is critical for efforts to reweight populations obtained from cryo-EM data, as absent conformations become unknowns.

We hypothesized that the kinetic connectivity of a state may categorize the extent of perturbation. To quantify this kinetic network, we defined an "event time" for each microstate (*Categorizing Changes Under Cooling with Hot Equilibrium Kinetics*),

$$\nu_k(t_M) = 0.05 \times 2t_M \underbrace{\left(\sum_{j,j\neq k} \pi_k(T) P_{kj} + \pi_j(T) P_{jk} \right)}_{=a_k(t_M)}^{-1}. \quad [1]$$

Here, ν_k is the event time for state k, t_M is the lagtime, $a_k(t_M)$ is the part of the dynamical activity contributed by state k at that lagtime, $\pi_j(T)$ is the equilibrium population of state j at temperature T, and P_{jk} is the transition probability for going from j to k with lagtime t_M, and the factor of 0.05 scales the quantity to be the amount of time needed to flow 5% of the system's total population. Broadly, we expect that states with slowest event times will be resistant to annealing. Note that almost all states with long event times are so kinetically isolated that they are estimated to be rare at equilibrium (*SI Appendix*, Fig. S9*A*). In our system, the states with the fastest event times are 24 and 27 (186 and 170 ns respectively), while the slowest event time (205 μs) is exhibited by state 31 (*SI Appendix*, Fig. S9*B*). We binned states according to their event time (Eq. **1**) and calculated the per-state contribution to the KL divergence (*Materials and Methods*) from the 277 K equilibrium distribution as a function of the cooling rate (Fig. 4*C*). At the fastest cooling rate, states exhibited almost no changes in population. As cooling slows, states with event times at or shorter than the cooling duration tend to show population changes.

Downloaded from https://www.pnas.org by PRINCETON UNIV LIBRARY; ACQUISITION SERVICE PERIODICALS on November 4, 2026 from IP address 140.180.240.79.

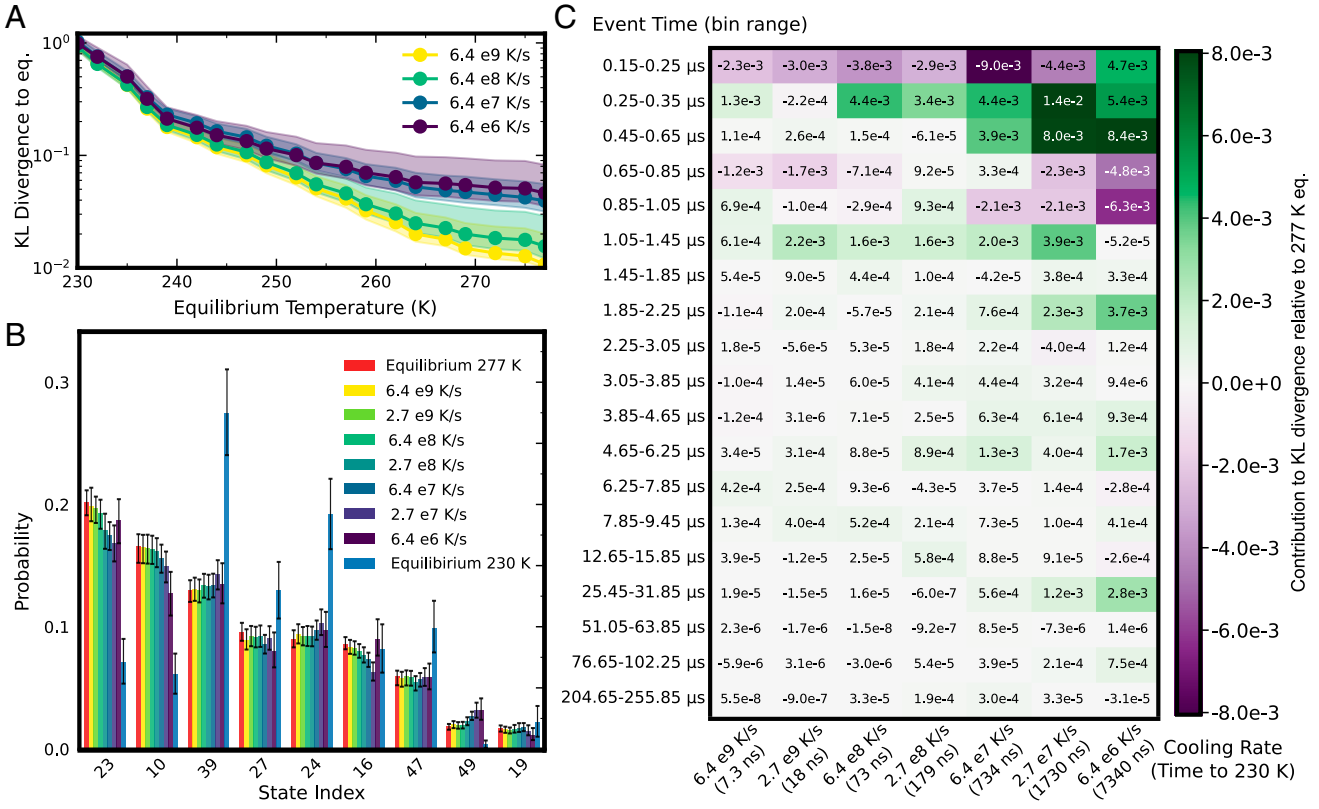


Fig. 4. Cooling rate-dependent changes to the conformational distribution of Trp-cage. (*A*) Kullback–Leibler (KL) divergence between cooled population distributions and equilibrium population distributions at each temperature from 277 K to 230 K, using the equilibrium distribution at each temperature as a reference. Each line represents a different cooling rate and shaded area represents 95% credible intervals. (*B*) State populations following vitrification at multiple cooling rates (colored bars) compared to equilibrium state populations at 277 K (red bars) and 230 K (blue bars). States with population >1% at 277 K are shown, ordered by equilibrium probability at 277 K. All 50 states can be found in *SI Appendix*, Fig. S9*A*. Error bars represent 95% credible intervals from Bayesian bootstrapping. (*C*) Heat map showing the relationship between states' event times, the cooling rate, and median change in that bin's contribution to the KL divergence between the equilibrium 277 K and cooled distributions, with the equilibrium as the reference. Numbers in the heat-map also report this value. States are binned together by their event times. See *SI Appendix*, Fig. S9*B* for a per-state heat map.

Changes to Protein Observables from Vitrification. Having characterized ensemble-level perturbations, we investigated how cooling affects protein structure. To probe structural changes beyond the resolution of our MSM (limited by its 40 ns lag time), we examined sidechain dihedral angles, which can undergo rotameric transitions on faster timescales. We focused on two representative residues: Asn1, a solvent-exposed asparagine at the N-terminus and Trp6, the tryptophan that forms the hydrophobic core. The χ_1 distribution of Asn1 shows clear cooling-rate dependence (Fig. 5*A*). At 277 K equilibrium, this sidechain primarily samples three rotameric states. After cooling, the distribution shifts toward gauche (+) with slower cooling rates, corresponding to the rotamer most favored at lower temperatures. In contrast, the χ_1 distribution of Trp6 remains essentially unchanged between hot equilibrium and all cooled ensembles (Fig. 5*B*). More generally, solvent-exposed residues tend to show cooling-rate-dependent sidechain reorientations, while buried residues in the hydrophobic core remain largely unaffected (*SI Appendix*, Figs. S10 and S11). Consistent with this, the ensembles we sample tend to be more compact, in terms of their R_g, at the slowest cooling rate we consider, but not as compact as the equilibrium 230 K limit (Fig. 5*C*).

Despite these global changes in compaction, the protein's hydrophobic packing remains largely intact. We quantified core structure by measuring sidechain–sidechain contacts between Trp6 and all other residues (Fig. 5*D*). The pattern of contacts in cooled ensembles closely matches the 277 K equilibrium across all cooling rates. Residues that make frequent contacts with Trp6 at 277 K, such as Pro12, Tyr3, and Pro18, maintain similar contact frequencies after cooling, while residues that rarely contact Trp6 at equilibrium remain unassociated in cooled ensembles.

Taken together, these structural analyses reveal that vitrification-induced changes concentrate in the flexible, solvent-exposed periphery of the protein. Slower cooling allows partial compaction and sidechain rearrangements in exposed regions as the system begins to relax toward more compact configurations accessible at reduced temperatures. However, these changes do not generally correspond to adoption of a different overall protein architecture, with the fold and hydrophobic core remaining broadly preserved, even while state populations are being affected by vitrification.

Thermodynamic Constraints Enable the Recovery of Equilibrium Populations from Cooled Ensembles. The observation of perturbed state populations resulting from vitrification motivated the development of a method to recover the equilibrium ensemble from a collection of cooled ensembles. Here, we developed an algorithm for thermodynamic inference based on bounds for entropy production derived from the principles of stochastic thermodynamics (20, 21). These thermodynamic constraints allowed us to determine the accessible equilibrium ensembles from the cooled distributions.

We studied the thermodynamics of nonequilibrium cooling by considering two distinct processes: the initial cooling, from

Downloaded from https://www.pnas.org by PRINCETON UNIV LIBRARY; ACQUISITION SERVICE PERIODICALS on November 4, 2026 from IP address 140.180.240.79.

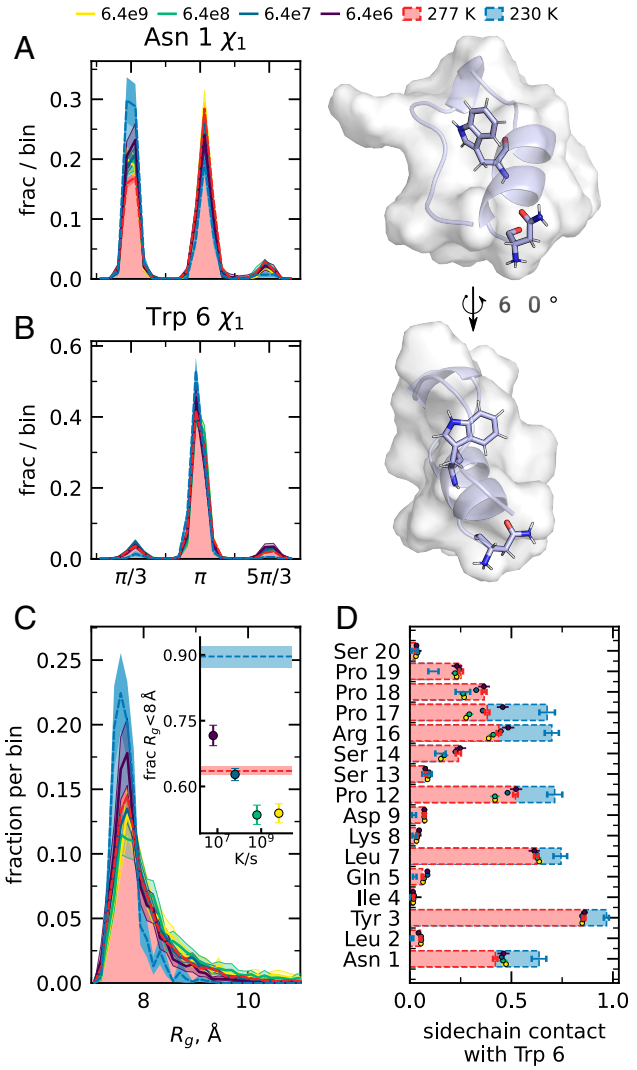


Fig. 5. Structural changes during vitrification localize to solvent-exposed regions while preserving the hydrophobic core. (*A* and *B*) Sidechain χ_1 dihedral angle distributions at equilibrium (277 K, red, and 230 K, blue) and after cooling at multiple rates (coloredlines) for (*A*) Asparagine 1, a solvent-exposed residue, and (*B*) Tryptophan 6, a buried core residue (both are shown in renders to the *Right*). Angles are shifted by π for easier visualization. Ribbons show error margin for each line. (*C*) Radius of gyration (R_g) distributions. As above, red and blue lines with error ribbons show equilibrium 277 K and 230 K R_g distributions; colored lines show cooled distributions. The *Inset* shows the maximum height of each histogram, on the Y axis. (*D*) Fraction of sidechain–sidechain contact between Trp6 and the rest of the protein, where contact is defined as any heavy atom within 4.5 Å. Colors and line-styles in all panels match the legend. Errors are 95% credibility intervals from bootstrapping of the weights.

time $t = 0$ at temperature $T_h = 277\,\mathrm{K}$ to time $t = \tau$ at temperature $T = 230\,\mathrm{K}$, and an auxiliary relaxation at temperature $T_c = 230\,\mathrm{K}$ from $t = \tau$ onward. At $t = 0$ the ensemble is the equilibrium Boltzmann distribution $\pi(T_h)$, while in the long time limit as $t \to \infty$ the ensemble will asymptotically approach the equilibrium distribution $\pi(T_c)$.

We modeled the cooled protein using master equation dynamics on a set of discrete states corresponding to the microstate MSM, each assumed to be characterized by state-dependent energy and entropy e_i and s_i. The state entropies account for the fact that the MSM microstates are not true microstates from a statistical mechanics standpoint (34). We do not explicitly model interactions between the protein and the solvent, however the state-dependent energies and entropies can implicitly account for such interactions.

We used stochastic thermodynamics (35) to compute the entropy production for the two processes under consideration. For each cooling time τ, the entropy productions Σ_{cool} and Σ_{aux} of the initial cooling and auxiliary relaxation processes, respectively, are functions of the state-dependent energies and entropies (both unknown), and the state probabilities at the end of the cooling process $p(\tau)$ (measured from experiments). The second law requires that entropy production of both the initial cooling process, as well as the auxiliary relaxation process, must be nonnegative for all cooling times τ:

$$\Sigma_{\mathrm{cool}}(\tau) \geq 0\,, \qquad \Sigma_{\mathrm{aux}}(\tau) \geq 0. \qquad [2]$$

We additionally took advantage of the data from multiple distinct cooling times by considering the relationships between entropy productions of cooling and relaxation for adjacent cooling times. We conjectured that the entropy production of the cooling process increases monotonically with cooling time, since for slower cooling rates the protein ensemble has more time to change and thus dissipate heat to its surroundings. Conversely, we conjectured that the entropy production of the auxiliary relaxation process decreases monotonically with cooling time, as slower cooling processes should yield ensembles closer to thermodynamic equilibrium at $T = 230\,\mathrm{K}$. By requiring monotonicity of entropy production, we obtained two additional inequality constraints for each pair of adjacent cooling times, thus taking advantage of the multiple cooling rates considered in this study. Specifically, for a set of n cooling times $\tau_1 < \tau_2 < \ldots < \tau_n$, we enforced

$$\Sigma_{\mathrm{cool}}(\tau_1) \leq \Sigma_{\mathrm{cool}}(\tau_2) \leq \ldots \leq \Sigma_{\mathrm{cool}}(\tau_n), \qquad [3a]$$
$$\Sigma_{\mathrm{aux}}(\tau_1) \geq \Sigma_{\mathrm{aux}}(\tau_2) \geq \ldots \geq \Sigma_{\mathrm{aux}}(\tau_n). \qquad [3b]$$

Details for calculating entropy production are in *Thermodynamic Constraints on Cooling*.

We then used the thermodynamic constraints to recover the initial equilibrium distributions, with an algorithm implemented as follows: first, we sampled points in the space of state entropies and valid probability distributions (satisfying normalization), then iterated differential evolution until all thermodynamic inequalities were satisfied. Repeating this process for many randomly-drawn initial points produced a sample of thermodynamically allowed distributions. This ensemble of allowed distributions is displayed through shading in Fig. 6*A*, which shows a projection of the state distribution onto two particular states. Lighter white indicates a higher density of sampled thermodynamically allowed distributions. We then obtained an estimated equilibrium distribution by taking the 10% of the thermodynamically allowed region closest to the fastest-cooled distributions, shown as the purple distributions with uncertainty in Fig. 6 *A* and *B*.

To demonstrate this thermodynamic recovery method, we first analyzed a toy model: overdamped diffusion of a Brownian particle in a two-dimensional potential energy landscape with six local minima (*SI Appendix*, Fig. S12*A*). For this model system, which showed nonmonotonic evolution of certain state probabilities with cooling time (*SI Appendix*, Fig. S12*B*), our method accurately recovered the full equilibrium ensemble using only the collection of simulated cooled ensembles (*SI Appendix*, Fig. S12*E*), obtaining a better estimate for the equilibrium ensemble than even the fastest simulated cooling time (*SI Appendix*, Fig. S12*F*).

Downloaded from https://www.pnas.org by PRINCETON UNIV LIBRARY; ACQUISITION SERVICE PERIODICALS on November 4, 2026 from IP address 140.180.240.79.

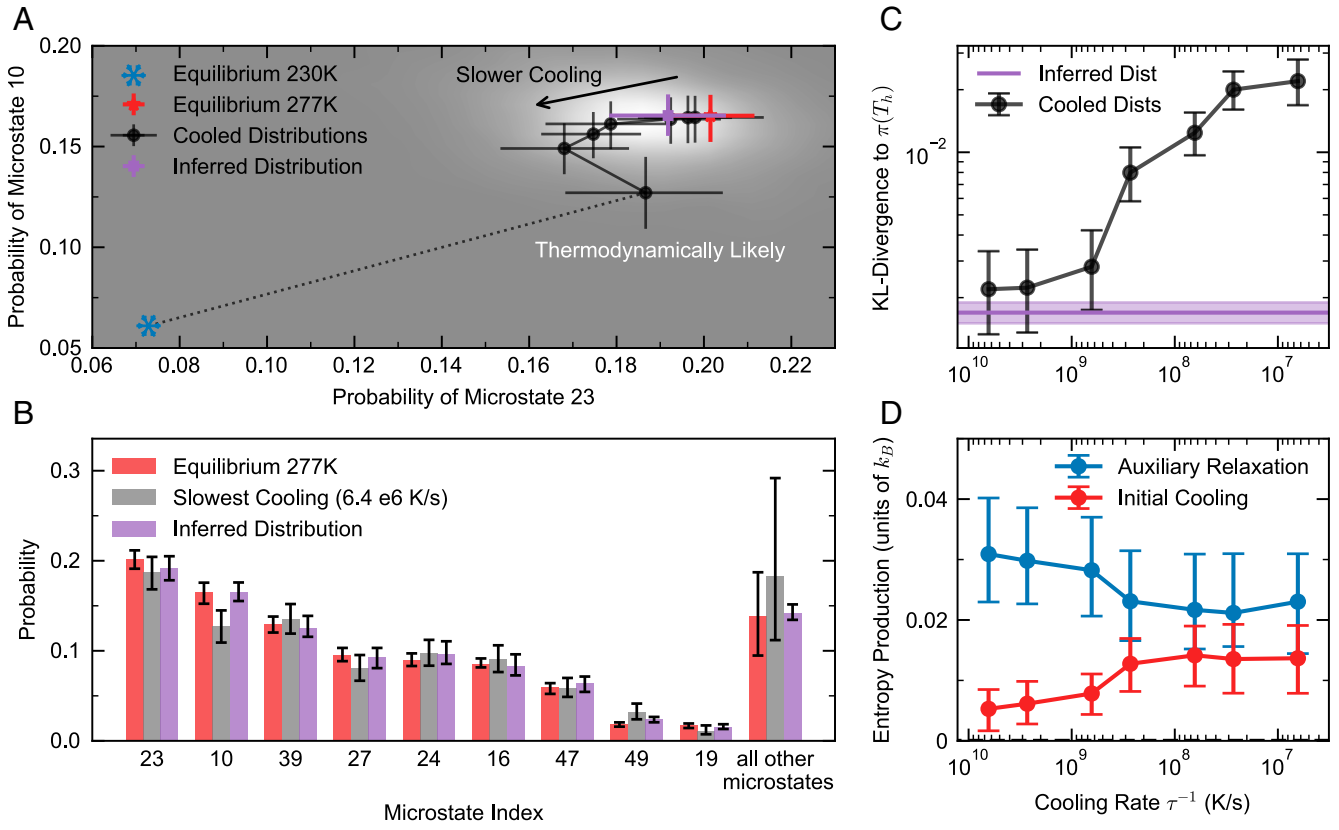


Fig. 6. Using thermodynamic constraints to recover the equilibrium ensemble from cooled distributions. (*A*) Projection of hot and cold equilibrium and cooled distributions onto the space of probabilities of microstates 10 and 23. (*B*) Histogram showing the true equilibrium distribution, cooled distribution with the slowest cooling time, and inferred distribution using all cooling times in the calculation. (*C*) KL-divergence for each nonequilibrium cooled distribution from the hot equilibrium distribution (black), as well as between the hot equilibrium distribution and the inferred distribution using all cooling times (purple). Light purple band indicates error bars. (*D*) Entropy production for the initial cooling process (upper bound, red) and auxiliary relaxation process (blue) as functions of the cooling rate τ^{-1}, computed using the inferred state probabilities and entropies.

We then applied the thermodynamic recovery method to our simulations of the Trp-cage protein to infer equilibrium state populations. Fig. 6*A* illustrates the thermodynamic recovery method applied to the microstate MSM, showing a two-dimensional projection of the thermodynamically allowed space of equilibrium ensembles, which contains the true equilibrium ensemble. This visualization shows the distribution moving away from the thermodynamically allowed region as the cooling time increases. The thermodynamic recovery method produced an estimate of the distribution for the initial hot equilibrium ensemble from the trajectory of cooled distributions. We recovered the true equilibrium probabilities for the nine most probable microstates in the MSM within uncertainty (Fig. 6*B*), and found that the inferred distribution is closer to the true equilibrium, as quantified by KL-divergence, than even the fastest-cooled distributions (Fig. 6*C*). The inferred entropy productions for both the initial cooling and auxiliary relaxation processes are nonnegative, and monotonic with cooling time as required by our thermodynamic constraints (Fig. 6*D*).

Since our fastest cooling rates are faster than realistic cooling processes used in cryo-EM, we also tested the recovery process using only data from the three slowest cooling runs. As in the case of using all coolings, our recovery method successfully recovered an inferred distribution closer to the true equilibrium than any of the three slowest-cooled distributions (*SI Appendix*, Fig. S13). While our thermodynamic recovery method performs best when multiple rank-ordered cooling times are available, it can still be applied using only data from a single cooling time by using only the nonnegativity constraints on entropy production (Eq. **2**). We tested this approach using only the data from the critical cooling rate, and found that while uncertainties are large, the resulting inferred distribution is nonetheless closer to the true hot equilibrium than the cooled distribution (*SI Appendix*, Fig. S14). These results show that our method can be applied even when multiple cooling rates are not available.

Discussion

Through extensive molecular simulation and a computational nonequilibrium statistical mechanics approach, this work creates a foundation for understanding the perturbative effects of the vitrification process in cryo-EM. First, we have shown that water glass formation is unperturbed by the presence of the Trp-cage, and likely other biomolecules as well. We found that susceptibility to annealing during cooling depends on a state's kinetic connectivity, with isolated states remaining more robust than well-connected ones. Perhaps most importantly, we show that even kinetically active conformations present at 277 K can be observed, though not with the correct populations, in the cooled ensemble. We build on this result to propose a thermodynamic inference approach to recover equilibrium populations from the cryo-EM ensemble. Thus we have shown that recovering the correct ensemble populations from cryo-EM, a task with implications ranging from drug design to understanding the drivers of key biological processes, is possible.

Downloaded from https://www.pnas.org by PRINCETON UNIV LIBRARY; ACQUISITION SERVICE PERIODICALS on November 4, 2026 from IP address 140.180.240.79.

Despite these strong conclusions, this work does not come without caveats. As with all classical simulations, we are limited by force field accuracy, and by design choices in biopolymer force fields; no protein force field we are aware of is tuned for accuracy in supercooled water. In the case of Trp-cage, our choice of amber03w for the protein forcefield was based on previous validation that it exhibited folding behavior consistent with experiment, and also showed a cold-denatured state (36–38). TIP4P/Ice represented the best compromise between cost and accuracy at 277 K and in the supercooled liquid (26). While TIP4P/Ice exhibits a higher apparent T_g than real water, the more relevant comparison is the temperature at which larger conformational rearrangements become strongly hindered. Real water shows a dynamical crossover near 233 K, and TIP4P/Ice places the corresponding crossover near 245 K (26, 39). Proteins likewise undergo a dynamical transition around 240 K, associated with suppression of hydration-water translational diffusion and large-amplitude anharmonic motions (40). Consistent with this shift, TIP4P/Ice's transport coefficients at a given nominal temperature are known to differ from experiment, though this resolves when temperature is expressed relative to each model's triple point. This suggests our simulated protein dynamics are mildly overdamped relative to real water at the same temperature, which is directionally conservative for our event-time argument. States that we identify as kinetically robust to cooling would remain so, or more so, under this correction. Taken together, this suggests that our choice of T_c captures a similar dynamical regime to real vitrification, even if the transition temperature is shifted upward in TIP4P/Ice.

By inspecting water mobility and bulk rate-dependent density-temperature trajectories with and without protein, we establish that the system is large enough that Trp-cage does not materially alter water vitrification at ambient pressure in our simulations. While this result is an important control for our study, it is also suggestive. Because our protein concentrations are high (approximately 17 mM) relative to those used in cryo-EM, one might suppose that if perturbations to glass formation were likely from solutes like proteins, we would have seen them. Therefore, it is reasonable to suspect that other changes to the sample composition, such as low to moderate ionic strength, buffers, or other macromolecules at experimental concentrations, will likewise not perturb water glass formation, in agreement with experimental assessments of this effect (41).

The sampling required to achieve our results, 50.4 ms of total simulation time for a 20-residue protein, highlights a key limitation of this computational approach. This sampling includes 5.4 ms of unbiased simulation at 277 K, 1.1 ms of TREX, and 44 ms for the nonequilibrium cooling simulations, of which 18.4 ms were of the slowest cooling rate. This does imply that studying real cryo-EM systems through direct simulation of the cooling, as we have done here, is likely unfeasible given current computing resources. The unbiased dataset resulted in a well-sampled counts matrix for our MSM, with the least connected state still sampling 132,455 out transitions and 134,714 in transitions in aggregate. Despite the extensive unbiased sampling from an already converged TREX starting distribution and using modern MSM approaches, we could not initially build an MSM that was thermodynamically consistent with our cooling simulations or the state probabilities from histogramming our TREX data. This motivated using the TREX to constrain our MSM which in turn led to a thermodynamically consistent MSM with our cooling data. These findings suggest that thermodynamic constraints may prove useful more generally as a tool to rule out implausible MSM candidates.

Our extensive MD simulations establish quantitative relationships between biomolecular kinetics and vitrification-induced perturbations in cryo-EM. States with event times exceeding the duration of cooling are preserved during vitrification. At the experimental critical rate (6.4×10^6 K/s), for our system, this corresponded to states with event times around 7 μs. While faster-exchanging states exhibit measurable population shifts, their extent is a function of the state event time and the cooling duration. These results imply that the common choice to equilibrate samples at 277 K before vitrification is a good one, because it minimizes cooling artifacts by reducing the cooling duration. However, for cryo-EM practitioners interested in the states of their system at higher temperatures, at 298 or 310 K, the results presented here might not hold, since cooling from 310 K to 277 K may cause more pronounced changes in the ensemble populations than cooling from 277 K to 230 K. We did not investigate this directly here due to the associated further increase in computational cost that this would entail, and view it as an important direction for future work.

Previous simulation work on vitrification in the context of cryo-EM (19) established the feasibility of studying vitrification with MD, though the large system size used in that work necessitated cooling rates between 10^9 and 10^{11} K/s. Though that work persuasively argues these cooling rates to match those a molecule might experience very close to the surface of the water glass, it is probably inconsistent with the larger share of particles an experimentalist may image and further emphasizes how an ensemble from cryo-EM data will subtend a range of cooling rates. Other simulations studying the impact of cryogenic temperatures on actin have recently been reported; like our study, preferences for certain configurations are observed to be sensitive to temperature (42). Our focus on Trp-cage enabled exhaustive sampling at experimentally realistic rates, revealing how conformational kinetics quantitatively determine preservation. Because our approach to estimating the sensitivity of a state to annealing is based on all the transition paths available to a molecule, it is hard to compare it to earlier estimates by Bock and Grubmüller, who find that barriers below ∼10 kJ/mol can be traversed during cooling (19), thus framing the problem in a quasi two-state fashion.

It has been previously shown that the rapid cooling used in most crystallography for structure determination is slow enough to permit rearrangements of the side chains of the crystallized protein away from the room temperature ensemble (43–45). This cooling usually happens over >1 ms, and is affected by the different solvent conditions as well as the protein crystal itself. We also observed side chain distribution changes within Trp-cage due to cooling (Fig. 5*A* and *SI Appendix*, Fig. S11). This suggests that the cooling duration in cryo-EM is long enough to perturb side chain rotamer equilibrium distributions. Internal residue contacts remained stable within our simulations but this analysis is limited by the size of Trp-cage (Fig. 5*C*). Similar behavior was reported by Bock and Grubmüller (19), who observed that fluctuations in the cooled ensemble were greater in residues closer to the surface of the biomolecule. This is despite the fact that their system is thousands of residues larger than ours and their use of the Amber99sb forcefield and SPC/E water model—indicating that these effects are likely agnostic to choice of forcefield.

Our thermodynamic recovery framework offers a path toward quantitative ensemble determination even when vitrification perturbs populations. While our method can be applied with only data from a single cooling rate, it performed best with data from multiple rank-ordered cooling rates. This could in principle be determined by estimating sample thickness across

Downloaded from https://www.pnas.org by PRINCETON UNIV LIBRARY; ACQUISITION SERVICE PERIODICALS on November 4, 2026 from IP address 140.180.240.79.

cryo-EM grids (19, 46). A key advantage of our inference approach, however, is that it does not require precise cooling rate measurements, only rank ordering. Happily, it also does not directly require any notion of state kinetics. Our derivation assumed that protein volume does not change with temperature in a state-dependent manner (supported by *SI Appendix*, Fig. S9), and that microstate energies and entropies are temperature-independent, which may not always be the case for coarse-grained states. Future work could seek to relax these assumptions to further generalize our approach. Realizing the potential of this approach requires experimental determination of molecular state populations from cryo-EM data, which is still an active area of methodological development (4, 47). The combination of emerging heterogeneity analysis methods with our thermodynamic recovery framework could enable routine quantitative ensemble reconstruction from vitrified samples. Finally, our recovery method explicitly accounts for uncertainty in the measured cooled state populations. As these uncertainties grow larger, the thermodynamically likely region (Fig. 6*A*) will similarly widen, such that the equilibrium state populations are less tightly constrained.

This study confirms that cryo-EM holds promise as a powerful quantitative technique for molecular biophysics. One area in which our results have direct implications is for time-resolved cryo-EM experiments (18) where experiments are approaching the microsecond time scale of vitrification itself (48) and cooling artifacts become potentially significant. Our framework provides both a criterion for when artifacts matter, and a method to correct for them when they do. Additionally, our recovery method inherently returns estimates for state-dependent internal energy and entropy of the protein that include uncertainty. These in principle are sufficient to compute temperature-dependent free energy landscapes for a subset of discrete states. More broadly, whether such heterogeneity can be resolved from cryo-EM data is fundamentally a measurement problem, set by imaging noise rather than by the underlying dynamics (49). While Trp-cage is below the conventional cryo-EM size limit, the conformational changes we describe also occur in larger, cryo-EM-amenable proteins, where resolving them is at the edge of current capability, which we expect to improve with ongoing hardware advances (50). Altogether, this work provides a path forward as conformational heterogeneity methods evolve, time-resolved methods move toward faster time resolution (48), and the understanding of the perturbative effects of rapid cooling outlined here will become increasingly relevant.

Materials and Methods

Molecular Dynamics. We used the Amber03w protein force field (36), which was previously shown to accurately capture cold denaturation in Trp-cage (15), with the TIP4P/Ice water model (26) for its accurate reproduction of water's physical properties near the freezing point. (27). All simulations were performed at atmospheric pressure using GROMACS 2024.1, using a Nosé-Hoover thermostat with coupling time of 0.2 ps and a Parrinello–Rahman barostat with compressibility of 4.5×10^{-5} bar^{-1} and coupling time of 1 ps (51–54). We solvated the first conformer from NMR structure PDB 1L2Y (24) in a periodic box with 3,240 water molecules and one neutralizing chloride ion, resulting in a box with approximate edge length of 4.7 nm (*SI Appendix*, section 2).

To obtain reference populations for Trp-cage at our temperatures of interest, we performed TREX across 90 replicas spanning 230 K to 520 K (55), each simulated for 12 μs, (1.08 ms aggregate). From each replica, the first 2 μs were excluded as equilibration, the remaining 10 μs used to compute equilibrium populations at each temperature.

We seeded unbiased MD simulations at 277 K from 750 cluster centers determined by RMSD-based C_α clustering using a Euclidean metric and the *k*-hybrid approach provided by the enspara library on our 277 K TREX trajectory (56). Each cluster center was initialized with a random velocity and we then simulated no fewer than 20 simulations of each cluster center. A provisional MSM was used to target additional sampling toward the 20 most populated prototype states (10 additional states each) and toward long-lived states that were poorly kinetically resolved. We ran most trajectories for 200 ns, with some extended to 500, 750, 1,000, and 2,000 ns, for an aggregate 5.4 ms dataset.

Cooling simulations at all but the slowest rate were seeded from the same 750 RMSD cluster centers, and cooled by decreasing the temperature of the thermostat in 1 K steps of increasing duration linearly between 277 and 230 K. Some rates included an additional set seeded from prototype MSM states, as above. (*SI Appendix*, Table S1). We ensured at least 10 replicas per state across our cooling rates, though most states were sampled far more (*SI Appendix*, Fig. S17). For our slowest cooling rate, we prioritized molecular states that were most variable under cooling and those predicted to be central nodes for probability flux, to maximize sampling within our compute budget (See *SI Appendix* for additional details).

Markov State Model Construction. To develop features, we extracted all sine- and cosine-transformed dihedrals from the equilibrium 277 K sampling using PyEMMA (57). Dimensionality reduction was done with time-lagged independent component analysis (TICA, deeptime package) retaining 90% of the kinetic variance (29, 58–61). We used Koopman-reweighting to account for the relatively short length of individual trajectory lengths (28). We built multiple featurizations with lag times ranging from 1 ns to 40 ns.

We used *k*-means clustering as implemented in deeptime to create MSM states. To determine the number of clusters, we performed a VAMP scan (8, 62, 63) to choose a "fittable" number of clusters. We trained maximum likelihood MSMs on 50% train-test splits of featurized data, then rescored the test split with the VAMP decomposition of the trained model. We selected featurization hyperparameters to validate by picking the largest ones with concordant train and test VAMP2 scores (*SI Appendix*, Fig. S16).

We validated our model and state-space choice with implied timescales plots from the Bayesian model estimator available in deeptime (30). We assigned the TREX data to these clusters and constrained the stationary distribution to the 277 K TREX populations during fitting. We selected models with implied timescales that increased smoothly and monotonically, plateauing as a function of lag time (64). Our final model has 50 microstates, a 25 ns TICA lag time, and a 40 ns MSM lag time (further workflow discussion *SI Appendix*, section 5).

Estimating the Distribution of Molecular States After Nonequilibrium Cooling Simulations. To calculate each state's postcooling abundance, we counted the fractional (histogram) weight each starting state contributed via its equilibrium probability, toward the state in which its trajectory ended. This can be thought of as tracking packets of probability from beginning to end of the cooling process. For the microstates, this calculation was performed using

$$\vec{h} = \sum_i \left(x_{a_i} \hat{a}_i \cdot \vec{\pi}\right) \hat{b}_i, \qquad [4]$$

where i indexes the cooling runs, and $\vec{h}$ are the histogram weights for the microstates after cooling. The redundancy of seeding from each state is $x_a = 1/n_a$ with n_a trajectories started from a, $\hat{a}_i$ and $\hat{b}_i$ are indicators for start and end states of cooling run i, and $\vec{\pi}$ are the equilibrium populations.

We used Bayesian bootstrapping for error estimates of these probabilities (65, 66). We multiplied the above by a weight sampled from a Dirichlet distribution of the appropriate dimensionality as the prior to produce 2,000 resampled cooling histograms, from which we reported means and 95% credibility intervals. Further cooling simulation and seeding details are in *SI Appendix*.

Categorizing Change Under Cooling with Hot Equilibrium Kinetics. To assess whether a state would change under cooling, we adapted the dynamical activity concept from the stochastic thermodynamics literature (22):

$$a(t) = \sum_{i \neq j} a_{ij}(t) = \sum_{i \neq j} p_i(t) P_{ij}(t), \qquad [5]$$

Downloaded from https://www.pnas.org by PRINCETON UNIV LIBRARY; ACQUISITION SERVICE PERIODICALS on November 4, 2026 from IP address 140.180.240.79.

where $a(t)$ is the dynamical activity at the model's lag time t, with transition probabilities $P_{ij}(t)$, state probabilities $p_i(t)$, and the indices i, j correspond to the start and end states for the transition probabilities. At equilibrium at temperature T and a particular lag-time t_M, we write $p(t_M)_k \to \pi_k(T)$; $P_{ij}(t_M) \to P_{ij}$, and the contribution of state k to the activity will be

$$a_k(t_M) = \sum_{j,j\neq k} \pi_k(T)P_{kj} + \sum_{i,i\neq k} \pi_i(T)P_{ik} \qquad [6]$$
$$= \sum_{j,j\neq k} \left(\pi_k(T)P_{kj} + \pi_j(T)P_{jk}\right).$$

Because our MSM obeys detailed balance, the two summed terms are equal, so we scale the dynamical activity by 1/2 and further by 0.05 to set a 5% threshold, defining the event time of state k at lag time t_M as $\nu_k(t_M) = \frac{2t_M}{a_k(t_M)} \times 0.05$.

This quantity is in units of time per unit probability, because the units of MSM step on the lag time and the dynamical activity both cancel. Thus, it is the time it would take, at equilibrium, for 5% of the total probability to flow out of state k.

To score per-state probability change between equilibrium and cooled distributions, we computed each state's contribution to the Kullback–Leibler divergence between the equilibrium and the cooled distribution,

$$D_k(\vec{\pi}(T_h)\,||\vec{p}(T_c,\tau_c)) = \log(\pi_k(T_h)/p_k(T_c,\tau_c)). \qquad [7]$$

where T_h is the hot temperature, T_c is the cold temperature, $\pi_k(T_h)$ is the hot equilibrium probability for state k, and $p_k(T_c,\tau)$ is the probability of state k after nonequilibrium cooling over time τ to temperature T_c.

Thermodynamic Constraints on Cooling. We model the protein as a discrete-state system with N states $\{x_i : i = 1,...,N\}$, evolving under a master equation with transition rates obeying local detailed balance at a monotonically decreasing but otherwise unknown temperature protocol $T(t)$ (full derivation in *SI Appendix*). The system is initialized at equilibrium at temperature $T(0) = T_h$, described by the Boltzmann distribution $\pi_i(T_h)$ with state-specific energies $\{e_i\}$ and entropies $\{s_i\}$. We assume the protein volume is state-independent, supported by analysis of the cooled protein ensemble (*SI Appendix*, Fig. S9). Further assuming $\{e_i\}$ and $\{s_i\}$ are temperature-independent, as is standard when modeling protein conformation distributions (67, 68), the cold distribution at $T_c < T_h$ is likewise Boltzmann-distributed, $\pi_i(T_c)$.

The temperature is rapidly and monotonically decreased over time τ to T_c, leaving the system in a nonequilibrium distribution $p_i(\tau)$. We also consider an auxiliary relaxation process from $t = \tau$ to $t = \infty$, in which the system relaxes to $\pi_i(T_c)$. Using stochastic thermodynamics (35), the entropy production for the auxiliary relaxation process is

$$\Sigma_{\text{aux}}(\tau) = S[\pi(T_c)] - S[p(\tau)] - (E[\pi(T_c)] - E[p(\tau)])/T_c, \qquad [8]$$

where $E[p] = \sum_i p_i e_i$ and $S[p] = \sum_i p_i(s_i - k_B \log p_i)$ (34). Because the initial cooling process has time-dependent $T(t)$, its entropy production cannot generally be evaluated exactly. By assuming the mean energy decreases monotonically with temperature, we obtain an upper bound

$$\Sigma^{\text{UB}}_{\text{cool}}(\tau) = S[p(\tau)] - S[\pi(T_h)] - (E[p(\tau)] - E[\pi(T_h)])/T_c. \qquad [9]$$

Both bounds depend only on energy/entropy differences, not the (unknown) partition functions.

Both processes must satisfy the second law Eq. **2**, giving two constraints per cooling time τ. We further conjecture, proved in the small-τ limit (SI) and supported by numerical experiments and prior work on nonequilibrium cooling (69–71), that entropy production for each process is monotonic in τ, giving Eq. **3**: $2(N-1)$ further constraints for N cooling times.

To estimate $\pi(T_h)$, we sample the thermodynamically likely region for $\{\pi_i(T_h)\}$ and $\{s_i\}$ via a differential evolution algorithm, using all cooled distributions $\{p(\tau)\}$. We then take the 10% of that region closest to the fastest available cooling times as our probability estimate (full algorithm details in *SI Appendix*).

Data, Materials, and Software Availability. Code to reproduce the main text figures is available on GitHub at https://github.com/flatironinstitute/cooling_fast_and_slow_2026 (72). Source code and documentation for the thermodynamic recovery algorithm are available at https://github.com/Matthew-Leighton/Cooling_Thermodynamic_Recovery (73). The molecular dynamics dataset has been deposited in Zenodo (https://doi.org/10.5281/zenodo.22087130) (74).

ACKNOWLEDGMENTS. The Flatiron Institute is a division of the Simons Foundation. We thank the Flatiron Scientific Computing Core, especially Geraud Krawezik for technical support, and the Folding@Home whose contributions enabled a portion of these simulations. Additional simulations used Princeton Research Computing resources, a consortium led by the Princeton Institute for Computational Science and Engineering and the Office of Information Technology's Research Computing. We thank R. Justin Lindsay for assistance with performing the replica exchange simulations, and Sukrit Singh and Erik Thiede for feedback on the manuscript. L.G.S. thanks Greg Bowman and Blanton Tolbert for support, and Alan Grossfield for helpful conversations. M.P.L. thanks Steven Blaber (University of British Colombia Physics) for helpful discussions, and Yale and The Natural Sciences and Engineering Research Council of Canada for fellowship support. S.K. acknowledges funding from Engineering and Physical Sciences Research Council (EP/X035603, EP/V030779) and St. Anne's College. R.C. acknowledges funding from Medical Research Council (MR/N013468 and MR/W00673), Magdalen College, and Oxford Department of Biochemistry M.A.A. is supported by a Gary Helman fellowship. Some authors made use of Claude Code and ChatGPT/Codex for organizing analysis pipelines, and for refining plotting scripts. All such work was manually reviewed for correctness.

Author affiliations: [a]Department of Biochemistry, University of Oxford, Oxford OX12JD United Kingdom; [b]Department of Biochemistry and Biophysics, University of Pennsylvania, Philadelphia, PA 19104; [c]Department of Physics, Quantitative Biology Institute, Yale University, New Haven, CT 06511; [d]Center for Computational Biology, Flatiron Institute, New York, NY 10010; [e]Department of Chemistry, Princeton University, Princeton, NJ 08544; [f]Department of Chemical and Biological Engineering, Princeton University, Princeton, NJ 08544; and [g]Center for Computational Mathematics, Flatiron Institute, New York, NY 10010

Author contributions: R.C., L.G.S., M.P.L., R.J.S., P.C., M.A.A., and S.M.H. designed research; R.C., L.G.S., M.P.L., R.J.S., and M.A.A. performed research; R.C., L.G.S., M.P.L., R.J.S., S.K., P.G.D., P.C., M.A.A., and S.M.H. analyzed data; and R.C., L.G.S., M.P.L., R.J.S., P.G.D., P.C., M.A.A., and S.M.H. wrote the paper.

Reviewers: L.V.B., Max Planck Institute for Multi disciplinary Sciences; H.G., Max Planck Institute for Multidisciplinary Sciences; and V.A.V., Temple University.

Competing interest statement: One of the co-authors, S.K., is a co-author with reviewer H.G. of a Comment that was published in 2025: (13) .

1. K. Henzler-Wildman, D. Kern, Dynamic personalities of proteins. *Nature* **450**, 964–972 (2007).
2. J. Dubochet *et al*., Cryo-electron microscopy of vitrified specimens. *Q. Rev. Biophys.* **21**, 129–228 (1988).
3. M. van Heel, J. Frank, Use of multivariates statistics in analysing the images of biological macromolecules. *Ultramicroscopy* **6**, 187–194 (1981).
4. M. A. Astore *et al*., The inaugural flatiron institute cryo-EM conformational heterogeneity challenge. bioRxiv [Preprint] (2025). https://doi.org/10.1101/2025.07.18.665582 (Accessed 7 October 2025).
5. W. S. Tang, E. D. Zhong, S. M. Hanson, E. H. Thiede, P. Cossio, Conformational heterogeneity and probability distributions from single-particle cryo-electron microscopy. *Curr. Opin. Struct. Biol.* **81**, 102626 (2023).
6. M. A. Astore, D. Silva-Sánchez, R. Blackwell, P. Cossio, S. M. Hanson, Comparing cryo-EM methods and molecular dynamics simulation to investigate heterogeneity in ligand-bound trpv1. *Nat. Commun.* **17**, 1067 (2025).
7. J. M. Mancl, X. Wu, M. Zhao, W. J. Tang, Dimerization and dynamics of angiotensin-i converting enzyme revealed by cryo-EM and md simulations. *eLife* **14**, 632263 (2025).
8. S. Chen *et al*., The dynamic conformational landscape of the protein methyltransferase SETD8. *eLife* **8**, e45403 (2019).
9. N. J. Mowry, C. R. Krüger, M. Drabbels, U. J. Lorenz, Direct measurement of the critical cooling rate for the vitrification of water. *Phys. Rev. Res.* **7**, 013095 (2025).
10. O. Mishima, L. Calvert, E. Whalley, 'melting ice' I at 77 K and 10 kbar: A new method of making amorphous solids. *Nature* **310**, 393–395 (1984).

Downloaded from https://www.pnas.org by PRINCETON UNIV LIBRARY; ACQUISITION SERVICE PERIODICALS on November 4, 2026 from IP address 140.180.240.79.

11. P. G. Debenedetti, F. H. Stillinger, Supercooled liquids and the glass transition. *Nature* **410**, 259–267 (2001).
12. G. P. Johari, A. Hallbrucker, E. Mayer, The glass-liquid transition of hyperquenched water. *Nature* **330**, 552–553 (1987).
13. R. E. Amaro *et al*., The need to implement FAIR principles in bimolecular simulations. *Nat. Methods* **22**, 641–645 (2025).
14. V. Munoz, M. Cerminara, When fast is better: Protein folding fundamentals and mechanisms from ultrafast approaches. *Biochem. J.* **473**, 2545–2559 (2016).
15. S. B. Kim, J. C. Palmer, P. G. Debenedetti, Computational investigation of cold denaturation in the Trp-cage miniprotein. *Proc. Natl. Acad. Sci. U.S.A.* **113**, 8991–8996 (2016).
16. N. Fischer, A. L. Konevega, W. Wintermeyer, M. V. Rodnina, H. Stark, Ribosome dynamics and tRNA movement by time-resolved electron cryomicroscopy. *Nature* **466**, 329–333 (2010).
17. C. Y. Chen, Y. C. Chang, B. L. Lin, C. H. Huang, M. D. Tsai, Temperature-resolved cryo-EM uncovers structural bases of temperature-dependent enzyme functions. *J. Am. Chem. Soc.* **141**, 19983–19987 (2019).
18. U. J. Lorenz, Microsecond time-resolved cryo-electron microscopy. *Curr. Opin. Struct. Biol.* **87**, 102840 (2024).
19. L. V. Bock, H. Grubmüller, Effects of cryo-EM cooling on structural ensembles. *Nat. Commun.* **13**, 1709 (2022).
20. U. Seifert, From stochastic thermodynamics to thermodynamic inference. *Annu. Rev. Condens. Matter Phys.* **10**, 171–192 (2019).
21. M. P. Leighton, D. A. Sivak, Flow of energy and information in molecular machines. *Annu. Rev. Phys. Chem.* **76**, 379–403 (2025).
22. T. Van Vu, K. Saito, Thermodynamic unification of optimal transport: Thermodynamic uncertainty relation, minimum dissipation, and thermodynamic speed limits. *Phys. Rev. X* **13**, 011013 (2023).
23. K. Lindorff-Larsen, S. Piana, R. O. Dror, D. E. Shaw, How fast-folding proteins fold. *Science* **334**, 517–520 (2011).
24. J. W. Neidigh, R. M. Fesinmeyer, N. H. Andersen, Designing a 20-residue protein. *Nat. Struct. Biol.* **9**, 425–430 (2002a).
25. D. J. Kozuch, F. H. Stillinger, P. G. Debenedetti, Low temperature protein refolding suggested by molecular simulation. *J. Chem. Phys.* **151**, 185101 (2019).
26. J. Abascal, E. Sanz, R. García Fernández, C. Vega, A potential model for the study of ices and amorphous water: Tip4p/ice. *J. Chem. Phys.* **122**, 234511 (2005).
27. S. Izadi, A. V. Onufriev, Accuracy limit of rigid 3-point water models. *J. Chem. Phys.* **145**, 074501 (2016).
28. H. Wu *et al*., Variational Koopman models: Slow collective variables and molecular kinetics from short off-equilibrium simulations. *J. Chem. Phys.* **146**, 154104 (2017).
29. G. Pérez-Hernández, F. Paul, T. Giorgino, G. De Fabritiis, F. Noé, Identification of slow molecular order parameters for Markov model construction. *J. Chem. Phys.* **139**, 015102 (2013).
30. B. Trendelkamp-Schroer, H. Wu, F. Paul, F. Noé, Estimation and uncertainty of reversible Markov models. *J. Chem. Phys.* **143**, 174101 (2015).
31. P. N. Patrone, A. Dienstfrey, A. R. Browning, S. Tucker, S. Christensen, Uncertainty quantification in molecular dynamics studies of the glass transition temperature. *Polymer* **87**, 246–259 (2016).
32. R. J. Szukalo, N. Giovambattista, P. G. Debenedetti, Computational investigation of water glasses using machine-learning potentials. *Proc. Natl. Acad. Sci. U.S.A.* **122**, e2509609122 (2025).
33. T. Loerting *et al*., How many amorphous ices are there?. *Phys. Chem. Chem. Phys.* **13**, 8783–8794 (2011).
34. M. Esposito, Stochastic thermodynamics under coarse graining. *Phys. Rev. E* **85**, 041125 (2012).
35. U. Seifert, Stochastic thermodynamics, fluctuation theorems and molecular machines. *Rep. Prog. Phys.* **75**, 126001 (2012).
36. R. B. Best, J. Mittal, Protein simulations with an optimized water model: Cooperative helix formation and temperature-induced unfolded state collapse. *J. Phys. Chem. B* **114**, 14916–14923 (2010).
37. S. B. Kim, C. J. Dsilva, I. G. Kevrekidis, P. G. Debenedetti, Systematic characterization of protein folding pathways using diffusion maps: Application to Trp-cage miniprotein. *J. Chem. Phys.* **142**, 085101 (2015).
38. Z. Ahmed, I. A. Beta, A. V. Mikhonin, S. A. Asher, UV-resonance Raman thermal unfolding study of Trp-Cage shows that it is not a simple two-state miniprotein. *J. Am. Chem. Soc.* **127**, 10943–10950 (2005).
39. R. Tyburski *et al*., Observation of a dynamic transition in bulk supercooled water. *Nat. Phys.* **22**, 21–26 (2026).
40. G. Schiro *et al*., Translational diffusion of hydration water correlates with functional motions in folded and intrinsically disordered proteins. *Nat. Commun.* **6**, 6490 (2015).
41. M. Warkentin, J. P. Sethna, R. E. Thorne, Critical droplet theory explains the glass formability of aqueous solutions. *Phys. Rev. Lett.* **110**, 015703 (2013).
42. S. Sridharan Iyer *et al*., Reaching the full potential of cryo-EM reconstructions with molecular dynamics simulations at 310 K: Actin filaments as an example. *Proc. Natl. Acad. Sci. U.S.A.* **122**, e2521421122 (2025).
43. T. R. Stachowski, M. Fischer, Unfreezing structural biology for drug discovery. *Nat. Chem. Biol.* **22**, 169–179 (2026).
44. B. Halle, Biomolecular cryocrystallography: Structural changes during flash-cooling. *Proc. Natl. Acad. Sci. U.S.A.* **101**, 4793–4798 (2004).
45. D. A. Keedy *et al*., An expanded allosteric network in ptp1b by multitemperature crystallography, fragment screening, and covalent tethering. *eLife* **7**, e36307 (2018).
46. J. Elferich, L. Kong, X. Zottig, N. Grigorieff, Ctffind5 provides improved insight into quality, tilt, and thickness of tem samples. *eLife* **13**, RP97227 (2024).
47. L. Evans *et al*., Counting particles in cryo-electron microscopy may result in incorrect population estimates. *Commun. Biol.* **9**, 421 (2026).
48. M. Haubner *et al*., Microsecond time-resolved cryo-EM based on jet vitrification. biorxiv [Preprint] (2025). https://doi.org/10.1101/2025.11.21.689681 (Accessed 24 March 2026).
49. H. H. Mattingly, L. Evans, P. Cossio, Measurement-limited learning of conformational heterogeneity in cryo-electron microscopy. arXiv [Preprint] (2026). https://arxiv.org/abs/2606.14449 (Accessed 12 June 2026).
50. P. N. Petrov *et al*., Laser phase plate improves structure determination of small proteins by cryo-EM. *Science* **393**, 195–199 (2026).
51. M. Parrinello, A. Rahman, Polymorphic transitions in single crystals: A new molecular dynamics method. *J. Appl. Phys.* **52**, 7182–7190 (1981).
52. S. Nosé, M. Klein, Constant pressure molecular dynamics for molecular systems. *Mol. Phys.* **50**, 1055–1076 (1983).
53. S. Nosé, A unified formulation of the constant temperature molecular dynamics methods. *J. Chem. Phys.* **81**, 511–519 (1984).
54. W. G. Hoover, Canonical dynamics: Equilibrium phase-space distributions. *Phys. Rev. A* **31**, 1695–1697 (1985).
55. Y. Sugita, Y. Okamoto, Replica-exchange molecular dynamics method for protein folding. *Chem. Phys. Lett.* **314**, 141–151 (1999).
56. J. R. Porter, M. I. Zimmerman, G. R. Bowman, Enspara: Modeling molecular ensembles with scalable data structures and parallel computing. *J. Chem. Phys.* **150**, 044108 (2019).
57. M. K. Scherer *et al*., PyEMMA 2: A software package for estimation, validation, and analysis of Markov models. *J. Chem. Theory Comput.* **11**, 5525–5542 (2015).
58. L. Molgedey, H. G. Schuster, Separation of a mixture of independent signals using time delayed correlations. *Phys. Rev. Lett.* **72**, 3634–3637 (1994).
59. Y. Naritomi, S. Fuchigami, Slow dynamics in protein fluctuations revealed by time-structure based independent component analysis: The case of domain motions. *J. Chem. Phys.* **134**, 065101 (2011).
60. C. R. Schwantes, V. S. Pande, Improvements in Markov state model construction reveal many non-native interactions in the folding of NTL9. *J. Chem. Theory Comput.* **9**, 2000–2009 (2013).
61. M. Hoffmann *et al*., Deeptime: A Python library for machine learning dynamical models from time series data. *Mach. Learn. Sci. Technol.* **3**, 015009 (2021).
62. A. Meller *et al*., Drug specificity and affinity are encoded in the probability of cryptic pocket opening in myosin motor domains. *eLife* **12**, e83602 (2023).
63. L. G. Smith, B. Novak, M. Osato, D. L. Mobley, G. R. Bowman, PopShift: A thermodynamically sound approach to estimate binding free energies by accounting for ligand-induced population shifts from a ligand-free Markov state model. *J. Chem. Theory Comput.* **20**, 1036–1050 (2024).
64. J. H. Prinz *et al*., Markov models of molecular kinetics: Generation and validation. *J. Chem. Phys.* **134**, 174105 (2011).
65. B. Mostofian, D. M. Zuckerman, Statistical uncertainty analysis for small-sample, high log-variance data: Cautions for bootstrapping and Bayesian bootstrapping. *J. Chem. Theory Comput.* **15**, 3499–3509 (2019).
66. D. B. Rubin, The Bayesian bootstrap. *Ann. Stat.* **9**, 130–134 (1981).
67. J. D. Bryngelson, P. G. Wolynes, Spin glasses and the statistical mechanics of protein folding. *Proc. Natl. Acad. Sci. U.S.A.* **84**, 7524–7528 (1987).
68. B. Ibarra-Molero, J. M. Sanchez-Ruiz, Statistical differential scanning calorimetry: probing protein folding-unfolding ensembles. *RSC Biomol. Sci.* (2008).
69. B. Andresen, J. Gordon, Optimal paths for minimizing entropy generation in a common class of finite-time heating and cooling processes. *Int. J. Heat Fluid Flow* **13**, 294–299 (1992).
70. G. Ibáñez, S. Cuevas, M. L. de Haro, Minimization of entropy generation by asymmetric convective cooling. *Int. J. Heat Mass Transf.* **46**, 1321–1328 (2003).
71. S. Stenholm, On entropy production. *Ann. Phys.* **323**, 2892–2904 (2008).
72. R. Clark *et al*., Data from "Cooling fast and slow: Characterizing the effects of vitrification in cryo-EM and the subsequent recovery of equilibrium populations." GitHub. https://github.com/flatironinstitute/cooling_fast_and_slow_2026. Deposited 24 August 2026.
73. M. P. Leighton, Cooling_Thermodynamic_Recovery: Reusable Python package for thermodynamic recovery algorithm. GitHub. https://github.com/Matthew-Leighton/Cooling_Thermodynamic_Recovery. Deposited 20 August 2026.
74. R. Clark *et al*., Data from "Cooling fast and slow: Characterizing the effects of vitrification in cryo-EM and the subsequent recovery of equilibrium populations." Zenodo. https://doi.org/10.5281/zenodo.22087130. Deposited 24 August 2026

Downloaded from https://www.pnas.org by PRINCETON UNIV LIBRARY; ACQUISITION SERVICE PERIODICALS on November 4, 2026 from IP address 140.180.240.79.